Localization of dislocation creep in the lower mantle: implications for the origin of seismic anisotropy

Allen K. McNamara [a],*, Shun-Ichiro Karato [b], Peter E. van Keken [a]

[a] *Department of Geological Sciences, 2534 C.C. Little Building, University of Michigan, Ann Arbor, MI 48109-1063, USA*
[b] *Department of Geology and Geophysics, 108 Pillsbury Hall, University of Minnesota, Minneapolis, MN 55455, USA*

Abstract

Recent seismological observations reveal the presence of seismic anisotropy in localized regions at the base of the mantle within an otherwise isotropic lower mantle. These regions can be placed in a tectonic context, corresponding to locations of paleosubduction and plume upwelling. This project works toward determining whether the observed seismic anisotropy may be explained by the development of a mineral fabric by lattice-preferred orientation (LPO). Numerical modeling is used to explore whether the conditions at the base of upwelling and downwelling regions are consistent with those required for fabric development. Specifically, we examine whether dislocation creep dominates these regions within a background mantle that flows primarily by diffusion creep. The key to our study is the use of a composite rheology that includes both mechanisms of diffusion and dislocation creep and is based on mineral physics experiments. Results show that it is possible to produce a localization of dislocation creep near slabs within a background mantle dominated by diffusion creep. In contrast, upwelling regions are characterized by a domination of diffusion creep. These results indicate that LPO may be the cause of lowermost mantle seismic anisotropy near paleoslabs, but other mechanisms such as shape-preferred orientation may be required to produce the anisotropy observed near upwellings. © 2001 Elsevier Science B.V. All rights reserved.

1. Introduction

A more detailed study of the lowermost mantle is needed to better understand the dynamical processes occurring at the core–mantle boundary (CMB) region. This region is particularly important because it likely includes a thermal boundary layer and may be a source of chemical heterogeneity as well (e.g. [1,2]). An improved understanding of the dynamics of this boundary region will allow us to work toward answering many fundamental questions regarding the dominant creep mechanisms in and near slabs and plumes, plume formation, slab deformation, the possible melt distribution, and the presence of chemical heterogeneity.

Recent improvements in seismic observations of

* Corresponding author. Tel.: +1-734-764-1435;
Fax: +1-734-763-4690.
E-mail addresses: mcnamar@umich.edu (A.K. McNamara), karato@tc.umn.edu (S.-I. Karato), keken@umich.edu (P.E. van Keken).

the CMB region (e.g. [3]) now allow additional constraints to be placed on geodynamical models. The focus of this project is to provide a first step in identifying the cause of the seismic anisotropy observed at the base of the mantle. Here, we investigate whether the observed anisotropy may be explained by the development of a mineral fabric caused by lattice-preferred orientation (LPO). We start by using numerical modeling to explore whether mantle conditions at upwelling and downwelling regions in the lowermost mantle are consistent with those required to develop a fabric. Specifically, we examine the degree of localization of dislocation creep near upwelling and downwelling regions in our models. Before discussing the details of the modeling, we will review the the seismic observations of and the mineral physics background on the mechanisms for the formation of seismic anisotropy.

1.1. Seismic observations

The bulk of the lower mantle is seismically isotropic except for some portions of D″ [4,5]. The observation of seismic anisotropy in the deepest mantle is important as it may be related to changes in mantle flow mechanisms or flow orientation. For example, seismic anisotropy in the upper mantle is generally considered to be due to LPO caused by dislocation creep in olivine [6].

Excellent summaries of the nature of D″ anisotropy are given in [3,7,8]. Studies of shear wave splitting have revealed the presence of anisotropy in patches of D″ beneath Alaska [9], the Caribbean [10], and the Indian Ocean [11] that can be interpreted as transverse isotropy with $V_{SH} > V_{SV}$ although the bias of source–receiver locations makes it difficult to rule out azimuthal anisotropy. A shear wave discontinuity 200–350 km above the CMB marks the onset of anisotropy in these regions, and there is evidence for a lack of anisotropy at shallower depths provided by the absence of shear wave splitting for source–receiver spacings at slightly smaller epicentral distances. Moreover, the magnitude of anisotropy decreases with depth, and becomes isotropic near the CMB. Furthermore, these regions are characterized by faster

than average wave velocities, hinting that they consist of paleosubducted slabs [12].

The pattern of anisotropy in the central Pacific is strikingly different. Seismic observations indicate a high degree of lateral variability with sub-regions exhibiting $V_{SV} > V_{SH}$, $V_{SH} > V_{SV}$, or no measurable anisotropy at all [13–17]. In contrast to the circum-Pacific regions, the anisotropy of the central Pacific appears to be deeper, just above the CMB, and there is no convincing evidence for a shear wave discontinuity. The presence of strong negative velocity gradients in the lowermost mantle, lower-than-average wave speeds regionally, a thick (∼40 km) ultralow-velocity zone (ULVZ), and a dense hotspot distribution at the surface all lead to the likelihood of this region being related to the source of mantle upwelling.

1.2. Causes of seismic anisotropy

The possible causes of seismic anisotropy at the base of the mantle are extensively summarized in [3,7,8,10,18–20].

Mantle anisotropy may be caused by either shape-preferred orientation (SPO) or LPO. SPO may be a result of either aligned melt inclusions or laminated solid materials with contrasting elastic properties. LPO is caused by an alignment of crystallographic axes of anisotropic minerals. Mineral physics studies have shown that the two main lower-mantle minerals, $(Mg,Fe)SiO_3$ and MgO, have a high degree of intrinsic anisotropy [20]. The development of LPO is closely linked to the creep mechanisms controlling flow. Diffusion creep dominates under low stress and/or small grain size and leads to a random distribution of mineral grain orientations resulting in an effectively isotropic aggregate. The observation that the bulk of the lower mantle is seismically isotropic is used to infer that diffusion creep is the primary flow mechanism operating [21].

On the other hand, dislocation creep occurs at high stresses and/or large grain sizes and leads to an alignment of mineral grains. The resulting aggregate is seismically anisotropic, the degree of which is dependent on the amount of strain.

2. Problem formulation

We are interested in determining the cause of lowermost mantle seismic anisotropy associated with upwellings and downwellings. We initially want to determine whether the anisotropy can be explained by the formation of a fabric by LPO. As a first step toward that goal, we investigate whether the conditions are appropriate for LPO development in upwelling and downwelling regions near the CMB by determining whether dislocation creep (LPO enhancing) or diffusion creep (LPO reducing) dominates in specific regions. To achieve this goal, we employ a composite rheology that includes components of diffusion and dislocation creep. We produce maps illustrating the relative influence of each component on the overall viscosity. Conditions are considered appropriate for fabric development if the dislocation creep component dominates the viscosity. We predict that regions dominated by dislocation creep have the potential to form a mineral fabric strong enough to produce the observed seismic anisotropy.

Since diffusion and dislocation creep are independent mechanisms, we utilize a composite rheology expressed as:

$$\dot{\varepsilon} = \dot{\varepsilon}_{\text{diff}} + \dot{\varepsilon}_{\text{disl}} \tag{1}$$

where $\dot{\varepsilon}_{\text{diff}}$ and $\dot{\varepsilon}_{\text{disl}}$ are the effective strain rates for diffusion creep and dislocation creep, respectively, and are expressed as:

$$\dot{\varepsilon}_{\text{diff}} = A'_{\text{diff}} \left(\frac{b}{d}\right)^m \exp\left(-\frac{g_{\text{diff}} \, T_{\text{m}}}{T_{\text{dim}}}\right) \frac{\sigma}{\mu} \tag{2}$$

$$\dot{\varepsilon}_{\text{disl}} = A'_{\text{disl}} \exp\left(-\frac{g_{\text{disl}} \, T_{\text{m}}}{T_{\text{dim}}}\right) \left(\frac{\sigma}{\mu}\right)^n \tag{3}$$

where A'_{diff} and A'_{disl} are prefactors, μ and b are reference values for the rigidity and Burgers vector, g_{diff} and g_{disl} are activation coefficients, T_{m} is the dimensional melting temperature, d is the grain size, σ is the stress, and m and n are constants. Because $\sigma = \eta\dot{\varepsilon}$, these may be rearranged to yield:

$$\eta = \left(\frac{1}{\eta_{\text{diff}}} + \frac{1}{\eta_{\text{disl}}}\right)^{-1} \tag{4}$$

where:

$$\eta_{\text{diff}} = \frac{\mu}{A'_{\text{diff}}} \left(\frac{d}{b}\right)^m \exp\left(\frac{g_{\text{diff}} \, T_{\text{m}}}{T_{\text{dim}}}\right) \tag{5}$$

$$\eta_{\text{disl}} = \frac{\mu}{A'_{\text{disl}}} \exp\left(\frac{g_{\text{disl}} \, T_{\text{m}}}{T_{\text{dim}}}\right) \left(\frac{\sigma}{\mu}\right)^{1-n} \tag{6}$$

where η is the effective viscosity, and η_{diff} and η_{disl} are the viscosities for the respective creep mechanisms.

The transition stress, σ_{t}, is defined as the stress at which the material flows equally by diffusion and dislocation creep:

$$\sigma_{\text{t}} = \left[\left(\frac{A'_{\text{disl}}}{A'_{\text{diff}}}\right) \left(\frac{d}{b}\right)^m \mu^{(1-n)} \exp \right.$$

$$\left. \left(\frac{T_{\text{m}}}{T} \left(g_{\text{diff}} - g_{\text{disl}}\right)\right) \right]^{\frac{1}{1-n}} \tag{7}$$

We employ an olivine rheology for the upper mantle ($g_{\text{diff}} = 17$, $g_{\text{disl}} = 31$). Rheological parameters for lower-mantle materials have large uncertainties; however, diffusion creep parameters are now relatively well constrained through direct experimental studies on MgO, (Mg,Fe)O, and $MgSiO_3$ perovskite [22]. Both materials have a relatively small activation coefficient for diffusion creep (g_{diff} is between 10 and 14). We use the lower value throughout ($g_{\text{diff}} = 10$). The activation coefficient for dislocation creep is less well constrained, and we have explored a range of this parameter from 10 to 18 [23].

The melting temperatures for both materials are parameterized as:

$$T_{\text{m}} =$$

$$2100 + 1.4848z - 5.00 \times 10^{-4} \, z^2 \text{ (upper mantle)} \tag{8}$$

$$T_{\mathrm{m}} =$$

$$2916 + 1.2500z - 165 \times 10^{-4}\,z^2 \;(\text{lower mantle})$$
(9)

where T is in Kelvin and z is the depth in km [22].

The viscosity prefactors, and consequently the transition stress, are not well known. We constrain these by choosing a set of prefactors that results in a background lower mantle dominated by diffusion creep, consistent with seismological observations. We also insist that the magnitude of average mantle viscosity is consistent with geoid and post-glacial rebound constraints [23]. In addition, experimental work on oxides limits the ratio of non-dimensional prefactors $A'_{\mathrm{disl}}/A'_{\mathrm{diff}}$ between 10^{-8} and 10^{-10} [24].

In order to simulate subduction of cold lithospheric slabs, we need a mechanism to break the rigid lid produced by the temperature-dependent rheology. We choose a method that utilizes a maximum yield stress in the topmost region of our model which is similar to that of [25]. In the upper 300 km of our model, the viscosity is adjusted in order not to exceed a critical yield stress, σ_{c} which is a function of depth. σ_{c} includes two components, a constant ductile yield stress, σ_{d}, and a depth-dependent brittle yield stress that is defined by a brittle stress gradient, σ'_{b}.

$$\sigma_{\mathrm{c}} = min(\sigma_{\mathrm{d}},\; \sigma'_{\mathrm{b}}z)$$
(10)

where z is the depth. The effective viscosity is defined as:

$$\eta_{\mathrm{eff}} = min\left(\eta(T, T_{\mathrm{m}}, \dot{\varepsilon}),\; \frac{\sigma_{\mathrm{c}}}{\dot{\varepsilon}} \right)$$
(11)

σ_{d} and σ'_{b} are related such that they are equal at a depth of 75 km. This implies that the brittle regime dominates near the surface and the ductile regime dominates at depth. Trial and error was used to pick appropriate values of σ_{d} that effectively produced slab-like features. We do not claim to adequately model the physical mechanisms occurring in the Earth's lithosphere, and we only use this method as a quasi-self-consistent method to break the rigid lid.

The list of fixed parameters used in this study is given in Table 1. Each run is started from a previous solution profile and is given enough time to reach a new quasi-equilibrium state. A successful model run must satisfy the constraint that the bulk of the lower-mantle flows primarily by diffusion creep. We attempt to meet the observational constraints of velocity, viscosity [23], and heat flow [26].

2.1. Model setup

The numerical calculations are performed by solving the non-dimensional conservation equations of mass, momentum, and energy in the extended Boussinesq approximation [27]. The equation for mass conservation in incompressible flow is:

$$\nabla \cdot \boldsymbol{u} = 0$$
(12)

where $\boldsymbol{u}$ is the velocity vector. The momentum equation is:

$$\nabla P + \nabla \cdot (\eta \underline{\dot{\varepsilon}}) = \alpha Ra T \hat{\boldsymbol{r}}$$
(13)

where $\hat{\boldsymbol{r}}$ is the radial unit vector directed toward the center, P is the dynamic pressure, η is the effective viscosity, $\dot{\varepsilon}$ is the deviatoric strain rate tensor, α is the non-dimensional thermal expansivity, Ra is the Rayleigh number, and T is the temperature. The energy equation includes viscous dissipation and adiabatic (de)compression:

$$\frac{\partial T}{\partial t} + (\boldsymbol{u} \cdot \nabla)T + \alpha \frac{T_{\mathrm{dim}}}{\Delta T} Diw = \nabla(k \cdot \nabla T) + \frac{Di}{Ra} \sigma_{ij} \frac{\partial u_i}{\partial x_j}$$
(14)

where t is time, T_{dim} is the dimensional temperature, k is the non-dimensional thermal conductivity, ΔT is the temperature contrast across the model, Di is the dissipation number, w is the radial component of velocity, σ_{ij} are components of the stress tensor, and u_i and x_i indicate the ith component of the velocity and location vectors, respectively. The strain rate components are:

$$\dot{\varepsilon}_{ij} = \frac{\partial u_i}{\partial x_j} + \frac{\partial u_j}{\partial x_i}$$
(15)

The second invariant of the strain rate tensor is the effective strain rate and is represented as:

$$\dot{\varepsilon} = (\tfrac{1}{2}\Sigma\dot{\varepsilon}_{ij}\dot{\varepsilon}_{ij})^{\frac{1}{2}} \qquad (16)$$

The Rayleigh number is given as:

$$Ra = \frac{\rho_0 g \alpha_0 \Delta T h^3}{\kappa_0 \eta_0} \qquad (17)$$

where ρ_0, α_0, κ_0, and η_0 are reference values of density, thermal expansivity, thermal diffusivity, and viscosity. h is the reference length scale corresponding to the depth of the mantle.

The non-dimensional viscosity is determined by dividing by the reference viscosity, η_0, which is defined as the diffusion creep viscosity of the olivine layer at $T_{\text{dim}} = 1500$ K and $z = 140$ km. The dissipation number is given as:

$$Di = \frac{\alpha g h}{C_p} \qquad (18)$$

We use depth-dependent values of thermal conductivity and thermal expansivity of the non-dimensional form:

$$k = \left[\frac{\rho}{\langle\rho\rangle}\right]^3 \qquad (19)$$

$$\alpha = \frac{1}{\rho^2} \qquad (20)$$

where ρ is the non-dimensional density given by:

$$\rho = \exp\left(\frac{Di}{\gamma}z'\right) \qquad (21)$$

where γ is the Grüneisen parameter (set equal to 1) and z' is the non-dimensional depth [28]. Note that the expression for variable density is only used in the specification of α and k. This parameterization is similar to that used in [29].

The equations are solved in a 2-D cylindrical geometry, and the model domain is a quarter cylinder. The radii of the bottom boundary, lower–upper-mantle interface, and top boundary are set to maintain the volume ratios of the Earth. Our models are bottom-heated in order to exaggerate the production of upwellings for study. The velocity boundary conditions are free slip.

The equations are solved with the finite element toolbox SEPRAN (http://dutita0.twi.tudelft.nl/sepran/sepran.html). The model domain is discretized into 21 356 nodal points. The momentum equation is solved on quadratic triangular elements using a penalty-function method [30]. The strain rate dependence of viscosity necessitates solving the momentum and viscosity equations iteratively until viscosity and velocity are consistent. In most cases a relaxation between successive velocity solutions is required. We do a pointwise iteration to determine stress in the viscosity calculation. A predictor–corrector method with upwinding is used to solve for temperature on linear triangular elements nested within the quadratic elements.

3. Results

Due to the uncertainty in the rheological parameters, we vary the lower-mantle dislocation creep activation coefficient, the magnitude of viscosity, and the transition stress. We also study the effect of weak slabs in the lower mantle.

Results are displayed as snapshots in time for particular model runs. Table 2 displays specific parameters used and output results for each presented run. Fig. 1 illustrates results from a model run which incorporates identical values of g for both diffusion and dislocation in the lower mantle. As a consequence, the transition stress for the lower mantle is independent of temperature and depth (Eq. 7). This run will be considered as a reference case that the other runs are compared to. The transition stress for this case is 70.7 MPa. The temperature field, shown in Fig. 1a, indicates the presence of upwelling jets of hot material at the edges as well as a cold slab penetrating into the lower mantle. Fig. 1b shows the corresponding viscosity field. The temperature-dependent rheology produces a slab that is much stiffer than the background mantle. The stress field, shown in Fig. 1c, indicates that regions of high stress are associated with the downwelling slab as

Table 1
Fixed parameters

Parameter	Description	Value	Units
ΔT	Temperature drop across mantle	3000	K
α_0	reference thermal expansivity	3×10^{-5}	K^{-1}
ρ_0	reference density	4500	kg m^{-3}
C_p	specific heat	1250	J kg^{-1} K^{-1}
h	mantle thickness	2.8×10^6	m
k_0	reference thermal conductivity	5.6	W m^{-1} K^{-1}
g	gravitational constant	9.8	m s^{-2}
κ_0	reference thermal diffusivity	$k_0\,\rho_0^{-1}\,C_p^{-1}$	
Di	dissipation number	0.5	
d_{um}	grain size	2.0	mm
d_{lm}	grain size	1.0	mm
m_{um}	grain size index	2.5	
m_{lm}	grain size index	2.5	
n_{um}	power-law index	3.0	
n_{lm}	power-law index	3.0	
$A'_{diff-um}$	olivine diffusion prefactor[a]	2.25×10^{14}	s^{-1}
$A'_{disl-um}$	olivine dislocation prefactor[a]	1.28×10^{22}	s^{-1}
$A'_{diff-lm}$	lower-mantle diffusion prefactor[a]	1.06×10^{14}	s^{-1}
μ	reference rigidity	300	GPa
b	Burgers vector	5.0×10^{-7}	mm
$g_{diff-um}$	olivine diffusion activation coefficient	17	
$g_{disl-um}$	olivine dislocation activation coefficient	31	
$g_{diff-lm}$	lower-mantle diffusion activation coefficient	10	
σ_d	ductile yield stress	400	MPa
σ'_b	brittle yield stress gradient	5.33	MPa km^{-1}
$R_{surface}$	non-dimensional surface radius	1.67813	
R_{bottom}	non-dimensional bottom radius	0.67813	
$R_{interface}$	non-dimensional upper–lower-mantle interface radius	1.42	
η_{max}	non-dimensional viscosity maximum	1.0	
η_{min}	non-dimensional viscosity minimum	10^{-6}	

Upper- and lower-mantle values are denoted by um and lm, respectively. The above radii are non-dimensionalized by dividing by the length scale, h.

[a] For the higher Rayleigh number case, $A'_{diff-um} = 9.01 \times 10^{14}$ s^{-1}, $A'_{disl-um} = 5.11 \times 10^{22}$ s^{-1}, and $A'_{diff-lm} = 4.22 \times 10^{14}$ s^{-1}.

well as the flanks of the upwellings. The logarithm of non-Newtonian (dislocation creep) viscosity over Newtonian (diffusion creep) viscosity is illustrated in Fig. 1d. Note that positive values represent regions of diffusion creep-dominated rheology whereas negative values represent regions where dislocation creep dominates. Dislocation creep dominates the upper mantle except for slab itself. The reason for a switch to diffusion creep in the upper mantle portion of the slab is that $g_{disl} > g_{diff}$ in the olivine rheology which results in an increased transition stress at lower temperatures (Eq. 7). In the lower mantle, diffusion creep dominates the background whereas dislocation creep is localized in and near the slab. In the thin space between the slab and the CMB, flow is dominated by diffusion creep, likely due to the free slip lower boundary condition and the low thermally activated viscosity which both in turn produce lower stresses. There are also smaller zones of dislocation creep-dominated rheology near the flanks of the upwellings.

We also investigated the effect of varying the transition stress while maintaining $g_{diff} = g_{disl}$. We performed runs with transition stresses of 32, 100, and 225 MPa. The case with $\sigma_t = 32$ MPa results in a slab that undergoes more intense dislocation creep-dominated flow. In addition, a large proportion (about half) of the lower mantle is dominated by dislocation creep. As the transi-

Table 2
Variable parameters and results

A'_{disl} (s^{-1})	(A'_{disl}/A'_{diff})	$g_{diff-um}$	$g_{disl-um}$	$g_{diff-lm}$	$g_{disl-lm}$	heat flow (mW m^{-2})	$\langle\eta\rangle_{log}$ (Pa s)	σ_T (MPa)	related figure
3.36×10^5	3.18×10^{-9}	17	31	10	10	53	1.8×10^{23}	70.7	Fig. 1
1.68×10^9	1.59×10^{-5}	17	31	10	14	50	1.9×10^{23}	197.2	Fig. 2
1.68×10^{14}	1.59×10^0	17	31	10	18	65	3.0×10^{23}	123.0	Fig. 3
3.36×10^{5a}	3.18×10^{-9}	17	31	10	10	58	1.4×10^{23}	70.7	Fig. 4
1.34×10^{6b}	3.18×10^{-9}	17	31	10	10	85	1.2×10^{23}	70.7	Fig. 5

A'_{disl}, (A'_{disl}/A'_{diff}), g_{disl}, $\langle\eta\rangle_{log}$, and σ_T, are lower-mantle values. $\langle\eta\rangle_{log}$ is the logarithmic average of viscosity. σ_T is evaluated at $T = 1800$ K and depth $= 2000$ km.
[a]Case in which the lower-mantle viscosity maximum is reduced to 0.1.
[b]Case in which the Rayleigh number is increased.

tion stress is increased, both the magnitude and the areal extent of dislocation creep domination is reduced. The case with $\sigma_t = 225$ MPa results in a thin sliver of dislocation creep-dominated behavior within the slab and near its base. In all cases, the base of upwelling regions remains in the diffusion creep regime.

Because of the uncertainty associated with the activation coefficient of the dislocation component of the lower-mantle rheology we have varied the value of g_{disl}. For unequal values of g_{diff} and g_{disl}, the transition stress depends on temperature and depth (Eq. 7). First, we varied g_{disl} while maintaining the prefactor ratio, A'_{diff}/A'_{disl}, used in the reference case. As g_{disl} was increased, the slab region became increasingly dominated by diffusion creep. With $g_{disl} = 12$, only tendrils of dislocation creep-dominated material remained near the slab. Greater values of g_{disl} resulted in flow that is entirely dominated by diffusion creep although in all cases, stress values remain similar to the reference case. The reason for this is that the transition stress (Eq. 7) increases greatly for small increases in g_{disl}. We reduced the prefactor ratio to provide lower transition stresses (Table 2). Temperature and viscosity ratio fields are shown in Figs. 2 and 3 for cases in which g_{disl} is increased and the prefactor ratio is decreased. In all cases we maintain the value of g_{diff} at 10. The consequence of $g_{disl} > g_{diff}$ is an increase in transition stress for decreasing temperature. Fig. 2a illustrates the temperature field for a case in which g_{disl} is set to 14. Compared to the reference case (Fig. 1), the style of convection is similar, but the viscosity ratio field (Fig. 2b) is markedly different.

The colder, central portion of the slab primarily undergoes diffusion creep, and dislocation creep is concentrated along the slab boundaries. In addition, dislocation creep is concentrated along the bending portion of the slab at the CMB, but as before, there is a thin gap between the CMB and the slab that flows mainly by diffusion creep. Fig. 3 shows results for a case in which g_{disl} is increased to 18. The temperature field is shown in Fig. 3a and the viscosity ratio field is shown in Fig. 3b. In this case, the cooler slab is almost entirely Newtonian, and localization of dislocation creep occurs mainly below the slab. In addition, the high-temperature dependence of dislocation creep has significantly decreased the transition stress in hot regions near the CMB and the upwellings, so flow is primarily non-Newtonian in these regions. Note however, the base of the upwelling regions remains dominated by diffusion creep.

Of some interest is the effect of reducing the stiffness of the slab in the lower mantle. As material passes through the transition zone into the lower mantle, recrystallization occurs. Karato et al. [31] have suggested that grain size is a function of temperature as it passes through the transition zone, so colder material will have a smaller grain size which acts to reduce viscosity. Fig. 4 illustrates results in which we have reduced the maximum viscosity cutoff by a factor of 10. The temperature and viscosity fields are shown in Fig. 4a,b, respectively. Note the sharp decrease in viscosity as the slab passes into the lower mantle. Examination of the viscosity ratio in Fig. 4c shows that regions where dislocation creep domi-
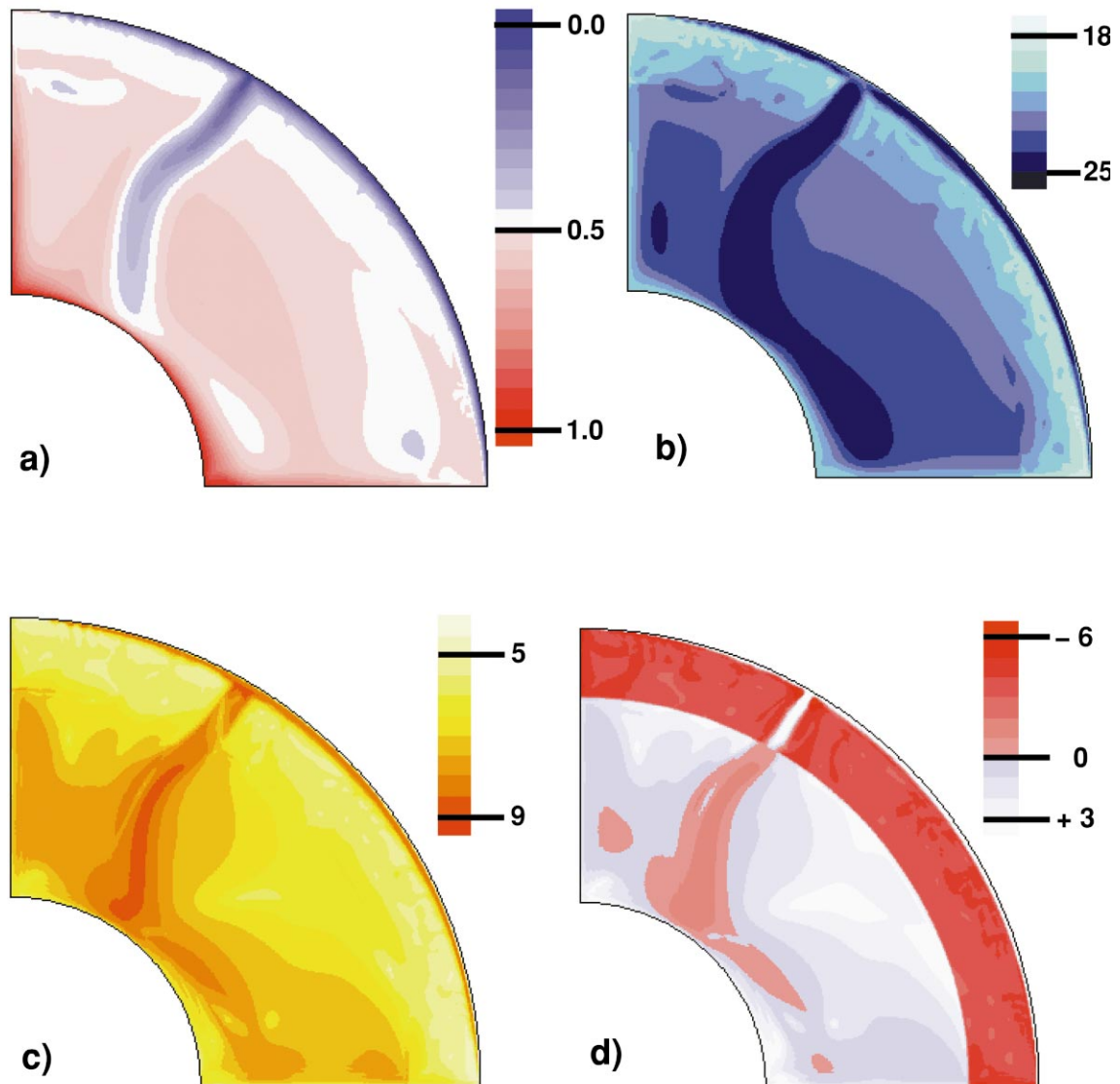
Fig. 1. Snapshot of a model run with $g_{diff} = g_{disl} = 10$ in the lower mantle, resulting in a transition stress that is independent of depth and temperature. (a) The temperature field shown in non-dimensional units. (b) The logarithm of dimensional viscosity in Pa s. (c) The logarithm of dimensional stress in Pa. (d) The logarithm of the ratio of non-Newtonian viscosity over Newtonian viscosity. Positive values (blue) reflect a domination of diffusion creep, and negative values (red) indicate a domination of dislocation creep.

nates are more widespread compared to the previous cases. Again, there is a thin band of diffusion dominated material directly above the CMB. We performed runs with a further reduction in the viscosity maximum and found similar results.

We performed a case at a higher convective vigor in order to examine the effect of lower over-all viscosity. We did this by uniformly decreasing the viscosity prefactors. Temperature and viscosity ratio fields are shown in Fig. 5a,b, respectively for one case. This more vigorous case results in an oscillatory migration of the subduction site, leading to the presence of a folded slab in the lower mantle. It is observed that the presence of a dis-
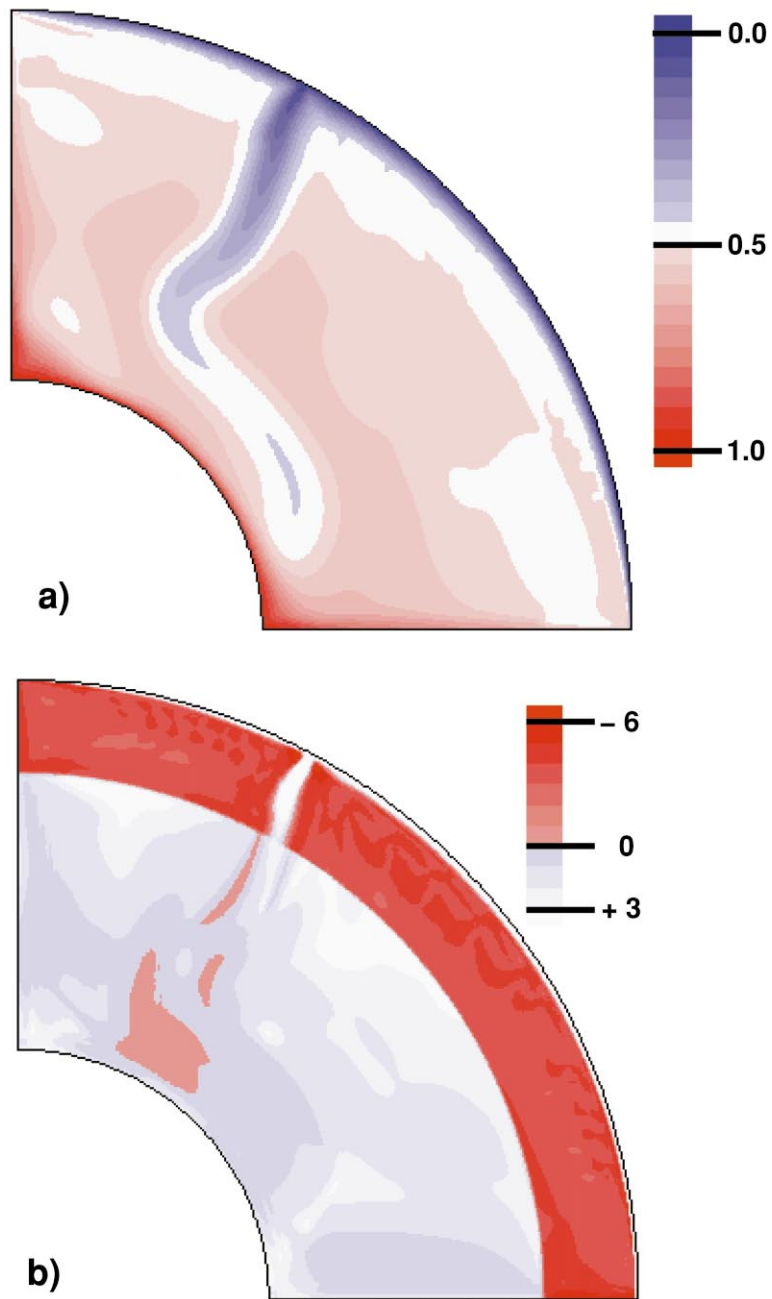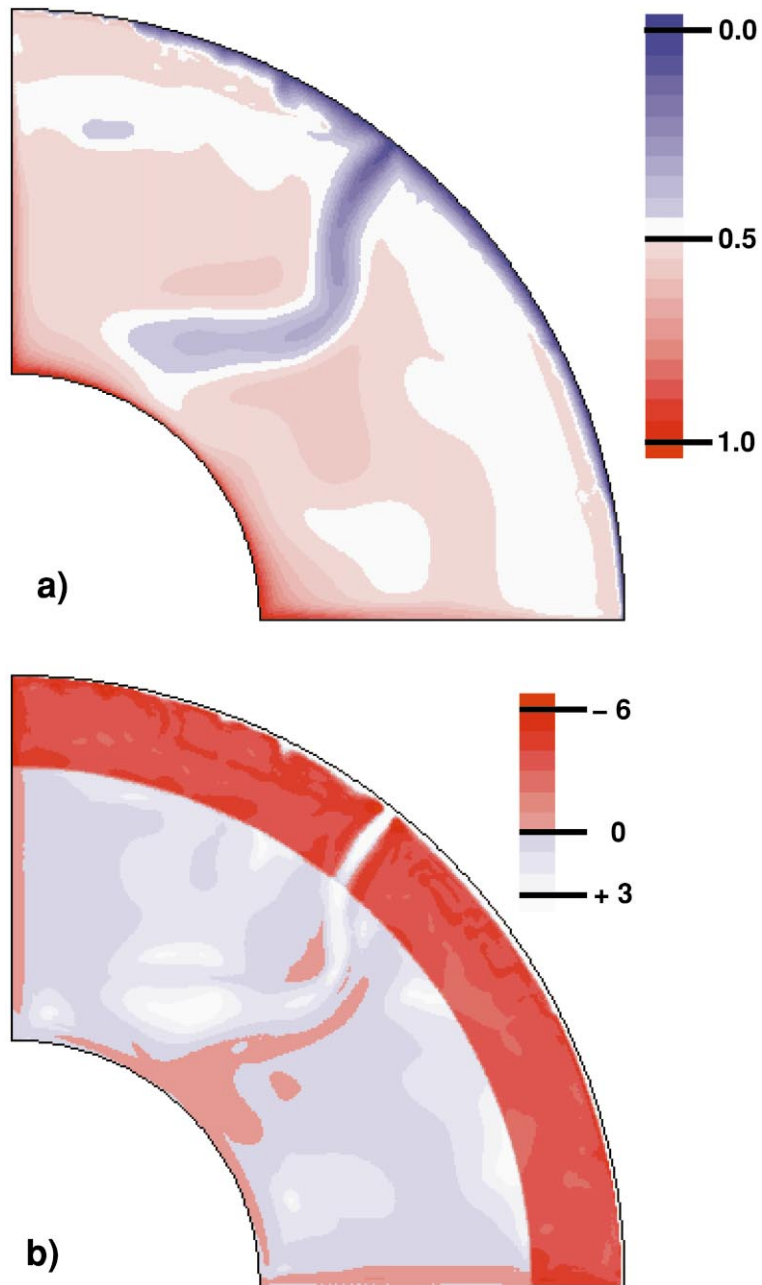
Fig. 2. Snapshot of a model run with $g_{diff} = 10$ and $g_{disl} = 14$ in the lower mantle. The transition stress increases with decreasing temperature. (a) The temperature field shown in non-dimensional units. (b) The logarithm of the ratio of non-Newtonian viscosity over Newtonian viscosity. Positive values (blue) reflect a domination of diffusion creep, and negative values (red) indicate a domination of dislocation creep.

Fig. 3. Snapshot of a model run with $g_{diff} = 10$ and $g_{disl} = 18$ in the lower mantle. The transition stress increases with decreasing temperature. (a) The temperature field shown in non-dimensional units. (b) The logarithm of the ratio of non-Newtonian viscosity over Newtonian viscosity. Positive values (blue) reflect a domination of diffusion creep, and negative values (red) indicate a domination of dislocation creep.
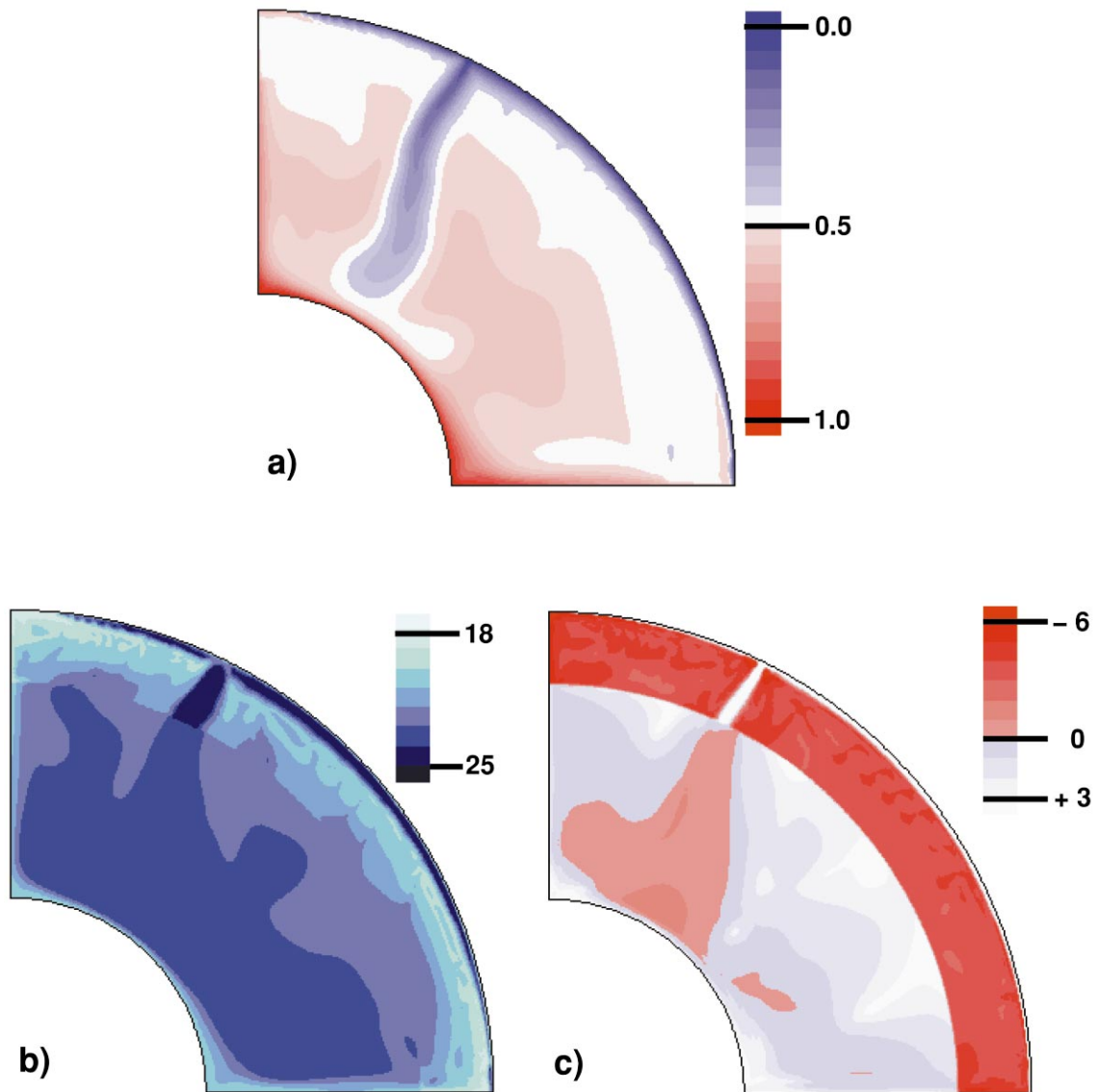
Fig. 4. Snapshot of a model run in which the maximum viscosity of the lower mantle has been reduced. $g_{diff} = g_{disl} = 10$ in the lower mantle. (a) The temperature field shown in non-dimensional units. (b) The logarithm of dimensional viscosity in Pa s. (c) The logarithm of the ratio of non-Newtonian viscosity over Newtonian viscosity. Positive values (blue) reflect a domination of diffusion creep, and negative values (red) indicate a domination of dislocation creep.

location creep-dominated region near the slab is preserved at higher convective vigor.

4. Discussion

The goal of this project was to use numerical modeling to determine if the conditions for fabric development by LPO are met near upwellings and downwellings at the base of the mantle under constraints of mineral physics, seismology, and surface observations such as heat flow, velocity, and viscosity. In essence, we were looking for high-stress regions that will allow a localization of dis-
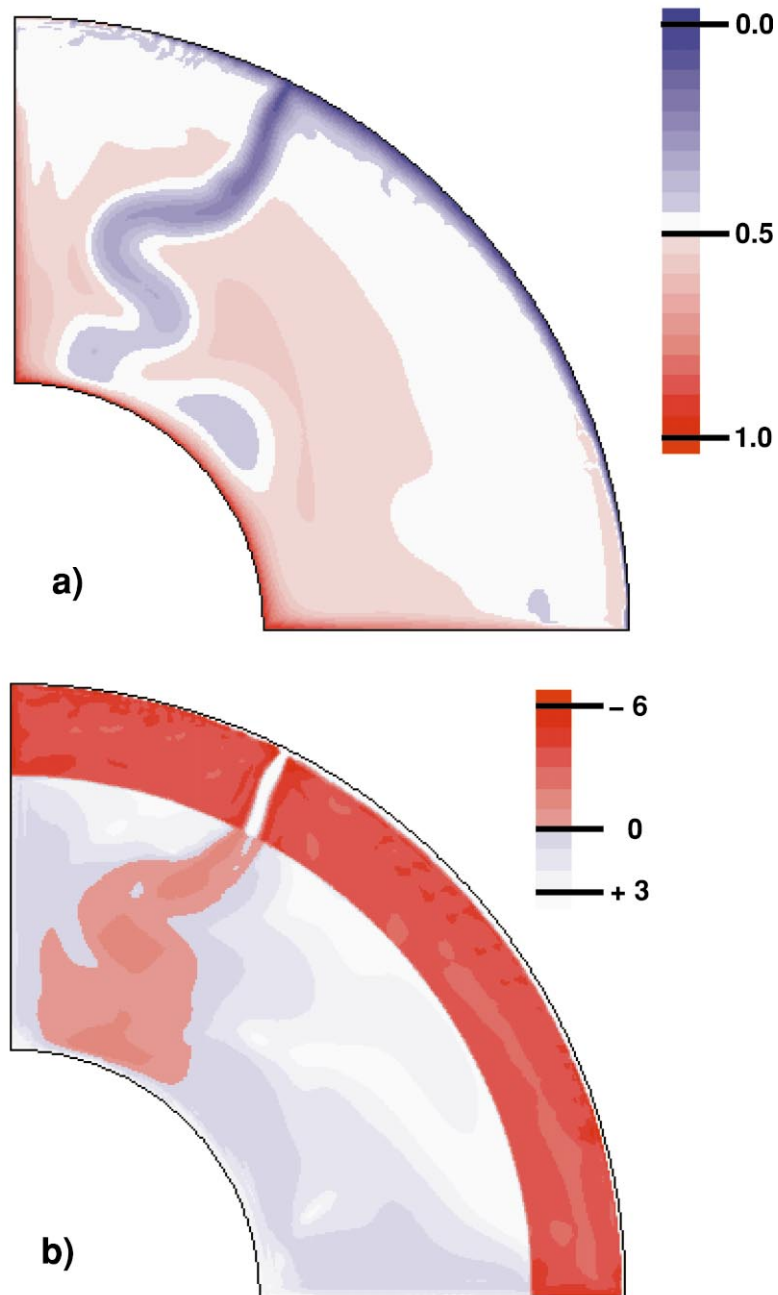
Fig. 5. Snapshot of a model run in which the viscosity prefactors have been uniformly decreased, resulting in a greater convective vigor. $g_{\text{diff}} = g_{\text{disl}} = 10$ in the lower mantle. (a) The temperature field shown in non-dimensional units. (b) The logarithm of the ratio of non-Newtonian viscosity over Newtonian viscosity. Positive values (blue) reflect a domination of diffusion creep, and negative values (red) indicate a domination of dislocation creep.

location creep in an otherwise diffusion creep-dominated mantle. Our results consistently reveal that slabs provide the highest stress regions in the lower mantle, leading to a localization of dislocation creep near downwellings. Therefore, conditions are right for the development of LPO in these regions and may provide the source of the observed seismic anisotropy. Interestingly, this was not observed at the base of upwellings. Our results show that hot upwelling regions are primarily Newtonian unless we significantly increase g_{disl}. Even under high g_{disl} values, only the plume conduits exhibit non-Newtonian flow, and the bases of the upwellings remain in the Newtonian regime. This result indicates that the conditions for LPO development are not right at the base of upwellings which is inconsistent with seismological observations [7] and leads to the possibility that SPO is the primary source of the observed anisotropy in these regions. These results indicate that it is important to look at stress regimes when using a temperature-dependent rheology rather than intuitively assuming fabric development in regions of high strain rate (e.g. [7]).

One point of consideration is how our results compare with the observation that seismic anisotropy ceases directly above D″. Most of our results reveal cases in which a domination of dislocation creep extends a considerable distance up the slab. Seismic observations are more robust near the CMB than other portions of the lower mantle, so a likely possibility is that seismology is insensitive to fabric development in much of the slab. Another possibility relates to the uncertainty in transition stress. Most of our model results indicate stress is greatest at the lowermost extent of the slab. If the transition stress is increased, it is conceivable that results with only a sliver of dislocation creep-dominated material will exist at the base of the mantle. An additional possibility is that the magnitude and direction of strain is not consistent with significant fabric development along the shallower portions of the slab. Preliminary calculations using model strain rates within the slab regions indicate that it takes approximately 1000 km of slab descent to produce 100% strain, an amount needed for the formation of a detectable fabric.

It is important to note that uncertainty in the ratio of rheological prefactors and the grain size of lower-mantle minerals allow for different volumetric extents of dislocation creep-dominated regions. We find that a larger A'_{disl}/A'_{diff} ratio or larger grain size extends the region exhibiting dislocation creep. Conversely, a smaller ratio or smaller grain size decreases the extent of dislocation creep-dominated regions. We consistently find that slabs provide the highest stress regions in our models and that the bases of upwellings are characterized by low stress. Diffusion creep is always the dominant flow mechanism at the base of upwellings, and dislocation creep dominates slab regions for transition stresses on the order of 250 MPa and less.

Our results show that localization of dislocation creep occurs in downwelling regions regardless of slab stiffness. To produce weak slabs we simply cut the maximum viscosity, but we admit that this may not be entirely appropriate. If the reasoning for weak slabs is smaller grain size, an increase in transition stress is expected. This may produce results more similar to those in which $g_{disl} > g_{diff}$. g Nevertheless, computational limitations make it computationally expensive to track a grain size field through the convection calculations.

We have shown that conditions are right for the development of LPO near slabs but not for upwellings. Future work which tracks the strain magnitude and direction is necessary for further constraining the degree of fabric development near slabs.

5. Conclusions

We used numerical modeling to examine whether conditions are appropriate for the development of LPO in upwelling and downwelling regions of the lower mantle. Specifically, we looked at whether mineral physics constraints on mantle rheology allow for regions of dislocation creep localization within a lower mantle that flows primarily by diffusion creep. Under a variation of the rheological parameters, we consistently observe slabs forming the highest stress regions, therefore, localization centers for dislocation

creep. In contrast, we observe hot upwelling regions to be dominated by diffusion creep. Our results indicate that the conditions are appropriate for the development of LPO in and near slabs. Our work also shows that it is unlikely that LPO is occurring in upwelling regions, and other mechanisms such as SPO may be required to explain the seismic anisotropy.

Acknowledgements

References

[1] R.W. Valenzuela, M.E. Wysession, Illuminating the base of the mantle with diffracted waves, in: M. Gurnis, M.E. Wysession, E. Knittle, B.A. Buffett (Eds.), The Core–Mantle Boundary Region, Geodynamics Series Vol. 28, AGU, Washington, DC, 1998, pp. 57–71.

[2] S. Karato, B.B. Karki, Origin of lateral variation of seismic wave velocities and density in the deep mantle, J. Geophys. Res., in press.

[3] T. Lay, Q. Williams, E.J. Garnero, The core–mantle boundary layer and deep earth dynamics, Nature 392 (1998) 461–468.

[4] C. Meade, P.G. Silver, S. Kaneshima, Laboratory and seismological observations of lower mantle isotropy, Geophys. Res. Lett. 22 (1995) 1293–1296.

[5] J.P. Montagner, B.L.N. Kennett, How to reconcile body-wave and normal-mode reference Earth models, Geophys. J. Int. 125 (1998) 229–248.

[6] A. Nicolas, N.I. Christensen, Formation of anisotropy in upper mantle peridotites – A review, in: K. Fuchs, C. Froidevaux (Eds.), Composition, Structure, and Dynamics of the Lithosphere-Asthenosphere System, Geodynamics Series Vol. 16, AGU, Washington, DC, 1987, pp. 111–123.

[7] T. Lay, Q. Williams, E.J. Garnero, L. Kellogg, M.E. Wysession, Seismic wave anisotropy in the D″ region and its implications, in: M. Gurnis, M.E. Wysession, E. Knittle, B.A. Buffett (Eds.), The Core–Mantle Boundary Region, Geodynamics Series Vol. 28, AGU, Washington, DC, 1998, pp. 299–318.

[8] J.M. Kendall, Seismic anisotropy in the boundary layers of the mantle, in: S. Karato, A.M. Forte, R.C. Liebermann, G. Masters, and L. Stixrude (Eds.), Earth's Deep Interior: Mineral Physics and Tomography From the Atomic to the Global Scale, Geophysics Monograph 117, AGU, Washington, DC, 2000, pp. 133–159.

[9] E.J. Garnero, T. Lay, Lateral variations in lowermost mantle shear wave anisotropy beneath the North Pacific and Alaska, J. Geophys. Res. 102 (1997) 8121–8135.

[10] J.M. Kendall, P.G. Silver, Constraints from seismic anisotropy on the nature of the lowermost mantle, Nature 381 (1996) 409–412.

[11] J. Ritsema, Evidence for shear velocity anisotropy in the lowermost mantle beneath the Indian Ocean, Geophys. Res. Lett. 27 (2000) 1041–1044.

[12] C. Lithgow-Bertelloni, M.A. Richards, The dynamics of Cenozoic and Mesozoic plate motions, Rev. Geophys. 36 (1998) 27–78.

[13] L. Breger, B. Romanowicz, Three-dimensional structure at the base of the mantle beneath the central Pacific, Science 282 (1998) 718–720.

[14] J. Ritsema, T. Lay, E.J. Garnero, H. Benz, Seismic anisotropy in the lowermost mantle beneath the Pacific, Geophys. Res. Lett. 25 (1998) 1229–1232.

[15] S.A. Russell, T. Lay, E.J. Garnero, Seismic evidence for small-scale dynamics in the lowermost mantle at the root of the Hawaiian hotspot, Nature 396 (1998) 255–258.

[16] L. Vinnik, L. Breger, B. Romanowicz, Anisotropic structures at the base of the Earth's mantle, Nature 393 (1998) 564–567.

[17] S. Russell, T. Lay, E.J. Garnero, Small-scale lateral shear velocity and anisotropy heterogeneity near the core–mantle boundary beneath the central Pacific imaged using broadband ScS waves, J. Geophys. Res. 104 (1999) 13183–13199.

[18] S. Karato, Some remarks on the origin of seismic anisotropy in the D″ layer, Earth Planets Space 50 (1998) 1019–1028.

[19] S. Karato, Seismic anisotropy in the deep mantle, boundary layers and the geometry of mantle convection, Pure Appl. Geophys. 151 (1998) 565–587.

[20] L. Stixrude, Elastic constants and anisotropy of $MgSiO_3$ perovskite, periclase, and SiO_2 at high pressure, in: M. Gurnis, M.E. Wysession, E. Knittle, and B.A. Buffett (Eds.), The Core–Mantle Boundary Region, Geodynamics Series Vol. 28, AGU, Washington, DC, 1998, pp. 83–96.

[21] S. Karato, S. Zhang, H. Wenk, Superplasticity in the Earth's lower mantle evidence from seismic anisotropy and rock physics, Science 270 (1995) 458–461.

[22] D. Yamazaki, S. Karato, Some mineral physics constraints on the rheology and geothermal structure of Earth's lower mantle, Am. Mineral. 86 (2001) 385–391.

[23] J.X. Mitrovica, A.M. Forte, Radial profile of mantle viscosity: results from the joint inversion of convection and postglacial rebound observables, J. Geophys. Res. 102 (1997) 2751–2769.

[24] H.J. Frost, M.F. Ashby, Deformation Mechanism Maps, Pergamon Press, Oxford, 1982, 167 pp.

[25] P.J. Tackley, Self-consistent generation of tectonic plates in time-dependent, three-dimensional mantle convection simulations: 1. Pseudoplastic yielding, Geochem. Geophys. Geosyst. 1,

[26] H.N. Pollack, S.J. Hurter, J.R. Johnson, Heat flow from the Earth's interior: analysis of the global data set, Rev. Geophys. 31 (1993) 267–280.

[27] J. Ita, S.D. King, Sensitivity of convection with an endothermic phase change to the form of governing equations, initial conditions, boundary conditions, and equations of state, J. Geophys. Res. 99 (1994) 15919–15938.

[28] G.T. Jarvis, D.P. McKenzie, Convection in a compressible fluid with infinite Prandtl number, J. Fluid Mech. 96 (1980) 515–583.

[29] A.M. Leitch, D.A. Yuen, G. Sewell, Mantle convection with internal heating and pressure-dependent thermal expansivity, Earth Planet. Sci. Lett. 102 (1991) 213–232.

[30] C. Cuvelier, A. Segal, A.A. Steenhoven, Finite element methods and Navier–Stokes Equations, Reidel, Dordrecht, 1986.

[31] S. Karato, M.R. Riedel, D.A. Yuen, Rheological structure and deformation of subducted slabs in the mantle transition zone: implications for mantle circulation and deep earthquakes, Phys. Earth Planet. Inter., in press.